Electronic Supplementary Material (ESI) for Nanoscale.

Full quantum search for high Tc two-dimensional van der Waals ferromagnetic semiconductors

Liang Liu[a,b], Zezhou Lin[a], Jifan Hu[c], Xi Zhang[a]*

a. Institute of Nanosurface Science and Engineering, Guangdong Provincial Key Laboratory of Micro/Nano Optomechatronics Engineering, Shenzhen University, Shenzhen 518060, China

b. Key Laboratory of Optoelectronic Devices and Systems of Ministry of Education and Guangdong Province, College of Optoelectronic Engineering, Shenzhen University, Shenzhen, 518060

c. School of Physics, State key laboratory for crystal materials, Shandong University, Jinan 250100, China

*e-mail address: zh0005xi@szu.edu.cn

In the supplementary information, we firstly provided the detail energy mapping method to extract Heisenberg parameters from DFT calculations. Secondly, the spin wave theory with interactions solved by Hatree-Fock approximations was introduced. Afterwards, the electronic and magnetic structures of five candidates were discussed in more details. The impactions of Hubbard U on d-shell were also presented. Finally, we verified our candidates on the level of GGA and discussed the performances of LDA, GGA and hybrid functionals approaches.

1. Determination of magnetic parameters in anisotropic Heisenberg model

In this part, we give the details of energy mapping method for the evaluation on the parameters in Heisenberg model (eq. 1 in main text) based on noncolinear DFT calculations.

Consider the case in which all spins point to x or y directions, the anisotropic terms of Heisenberg model vanish, leading to following energy expression:

$$E_i^{x(y)} = E_0^{x(y)} + \frac{S^2}{2}\sum_d F_i(d)J^{x(y)}(d) \qquad (S1)$$

where $E_i^{x(y)}$ is the calculated total DFT energy of system converged to ith type of spin configurations in which all spins point to ±x(y) direction. $F_i(d) = F_{FM}^{\ i}(d) - F_{AFM}^{\ i}(d)$ count the quantity difference between dth nearest neighbored (dNN) FM bonds and AFM bonds. FM bonds are bonds linking parallel spins pairs while AFM bonds are opposite. Apparently, eq. S1 can be uniquely determined with D+1 different magnetic configurations if we cutoff the exchange coupling at Dth NN.

The energy expression of z-oriented spin configuration is:

$$E_i^z - E_0 = NA_zS^2 + \frac{S^2}{2}\sum_d F_i(d)J^z(d) \qquad (S2)$$

where N is the number of magnetic ions involved in calculations. Since we have already obtained E_0 in eq. S1, this equation can also be uniquely solved using D+1 different magnetic

configuration. After some straight algebra, and noting that we have defined $J=(J^x+J^y)/2$, $B=J^z-J$, we can get all parameters in anisotropic Heisenberg Hamiltonian.

2. Hatree-Fock renormalized spin-wave

In this part we give the details of renormalized spin-wave solutions where interactions were approximately incorporated by Hatree-Fock method. To clearly describe the cases in which each cell consists of two or more magnetic ions, we re-express the Heisenberg Hamiltonian the eq. 1:

$$H=N\left\{\sum_{d\alpha\beta}J_{d\alpha\beta}(S_{0\alpha}^{z}S_{d\beta}^{z}+\frac{1}{2}(S_{0\alpha}^{+}S_{d\beta}^{-}+S_{0\alpha}^{-}S_{d\beta}^{+}))+\sum_{d\alpha\beta}B_{d\alpha\beta}S_{0\alpha}^{z}S_{d\beta}^{z}+A_z\sum_{\alpha}(S_{0\alpha}^{z})^2\right\}+E_0 \qquad (S3)$$

where d labels the index of cell, and α,β label the different magnetic ions in each cell. N is the quantity of cells in consideration. The translation symmetry is implicitly involved in eq. S3.

With Dyson-Maleev operator substitution discussed in main text, eq. S3 was reduced to the summation of two parts: H=H_0+H_1+const., where H_0 describes the free part of spin wave with quadratic expression:

$$H_0=-NS\left(\sum_{d\alpha\beta}(J_{d\alpha\beta}+B_{d\alpha\beta})n_{d\beta}-J_{d\alpha\beta}b_{0\alpha}^{\dagger}b_{d\beta}\right)-2NA_zS\sum_{\gamma}n_{0\gamma} \qquad (S4)$$

while H_1 describes the interactions between spin waves with quartic expression:

$$H_1=\frac{N}{2}\left(\sum_{d\alpha\beta}(J_{d\alpha\beta}+B_{d\alpha\beta})n_{0\alpha}n_{d\beta}-J_{d\alpha\beta}b_{0\alpha}^{\dagger}n_{0\alpha}b_{d\beta}\right)+NA_z\sum_{\gamma}n_{0\gamma}^2 \qquad (S5)$$

Within Fourier transformation $b_{i\alpha}^{\dagger}=\frac{1}{\sqrt{N}}\sum_{k}e^{-ikR_i}b_{k\alpha}^{\dagger}$, we obtain the free part of spin wave:

$$H_0=-S\sum_{k\alpha\beta}(J(0;\alpha\beta)+B(0;\alpha\beta))n_{k\alpha}-2AS\sum_{k\alpha}n_{k\alpha}+S\sum_{k\alpha\beta}b_{k\alpha}^{\dagger}J(k;\alpha\beta)b_{k\beta} \qquad (S6)$$

where k labels the wave vector, and $J(q;\alpha\beta)=\sum_{d}e^{iqd}J(d;\alpha\beta)$, $B(q;\alpha\beta)=\sum_{d}e^{iqd}B(d;\alpha\beta)$.

Up to Hatree-Fock approximation, the quartic part H_1 was approximated as:

$$H_1 = \frac{1}{N}\sum_{k\gamma k_1}\left\{J(k-k_1;\gamma\gamma) + B(k-k_1;\gamma\gamma) - J(k_1;\gamma\gamma) + 4A + \sum_{\alpha}(J(0;\alpha\gamma) + B($$
$$+ \sum_{k\gamma} An_{k\gamma} \qquad (S7)$$

here $\langle \bar{n}_{k_1} \rangle$ is the average occupation number on k_1 according to Bosons' distribution: $\langle \bar{n}_{k_1} \rangle = \left(e^{\beta\varepsilon_k} - 1\right)^{-1}$ where ε_k is the energy of spin wave and $\beta = 1/\kappa T$ is the inversed temperature. To further simplify the expression, we only consider the interactions between of Γ-wave and others, i.e. set $k_1 = 0$ in eq. S7. Therefore:

$$H_1 = \langle n \rangle \sum_{k\gamma}\left\{J(k;\gamma\gamma) + B(k;\gamma\gamma) - J(0;\gamma\gamma) + 4A + \sum_{\alpha}(J(0;\alpha\gamma) + B(0;\alpha\gamma))\right\}n$$
$$+ \sum_{k\gamma} An_{k\gamma} \qquad (S8)$$

here $\langle n \rangle$ is the average occupation of spin wave excitons over all k-points, governing by the Boson-Einstein distribution:

$$\langle n \rangle = \frac{1}{N}\sum_{k}\frac{1}{e^{\beta\varepsilon_k} - 1} \qquad (S9)$$

The summation is over irreducible Brillouin zone (iBZ). Since the total Hamiltonian $H = H_0 + H_1$ is renomalized by the interacting term H_1, it leads to the self-consistent problem and can be solved via scanning the value of $\langle n \rangle$ to see if and where the solution exists.

3. Detail electronic and magnetic structures of candidates

3.1 CrI_3

As shown in Fig. S1(a), Cr^{3+} ions are located at the center of octahedron formed by six I^-, leading to the splitting of e_g and t_{2g} orbitals. The octahedron is only slightly deformed, and Cr-I-Cr bond angles turn out to be ~98° in our fully optimized structures. Therefore, there are considerable

overlaps between e_g orbitals of Cr^{3+} and p_{xy} orbitals of I^-, as demonstrated by the Projected density of states (PDOS) in Fig. S1(b). This kind of electronic configuration supports FM type super-exchange mechanism between Cr^{3+}. Considering one of the Cr^{3+}- I^-- Cr^{3+} local structure, one p_x and one p_y electron of I^- hop to near two Cr^{3+} respectively, and they prefer the same spin orientation to reduce the onsite interactions i.e. the Hubbard interactions in p-shell of I ions. If the two Cr^{3+} have the same spin structure then exited structure will obey Hund's rule thus also minimize the exchange energy of excited Cr^{3+}, that is, ferromagnetic couplings between Cr ions are energetically favored from the 4nd order perturbation consideration. The lowest excited state can be formally represented as: $Cr(t_{2g\uparrow}^3)(p_x\text{-}e_{g\uparrow})I(p_{x\downarrow}p_{y\downarrow})(p_y\text{-}e_{g\uparrow})Cr(t_{2g\uparrow}^3)$, in which the p states of I^- are spin-polarized with reversed spin-orientation comparing to Cr^{3+}. This consideration is verified by the spin density in Fig. S1(a), where some down-spin densities on I^- were presented while the spin densities on surrounding Cr^{3+} were up-orientated. Since the relativistic effects around heavy Te elements are very large, these spin-polarized states of Te are sufficiently important in the crystalline anisotropies of magnetism, which was also found in other study very recently.[1, 2]

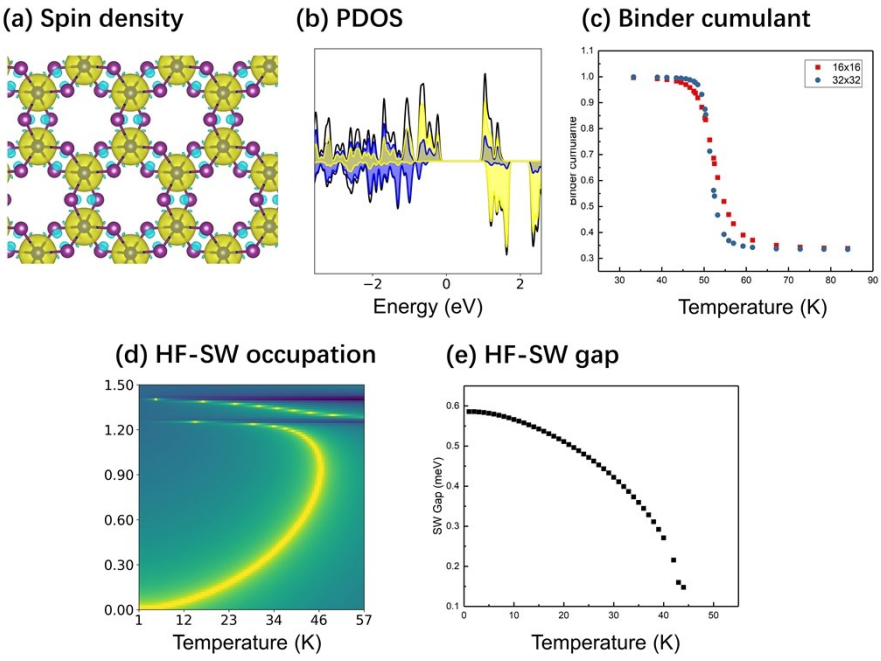

Fig. S1 (a) The spin density of CrI_3, yellow and blue surfaces correspond to up- and down-spin density, respectively. (b) Projected density of states of CrI_3. Blue and yellow shaded regions correspond to the DOS projected to p_{xy} and t_{2g} atomic orbitals. (c) Binder Cumulates vs. temperature obtained by QMC on 16x16 (red) and 32x32 (blue) sized CrI_3 supercells. (d) Hartree-Fock renormalized spin-wave occupations and (e) spin-wave gap under each temperature for CrI_3. The lightest area corresponds to the parameter space that can self-consistently solve the eq. S4-S9.

Fig. S1(d) shows the self-consistent solutions of occupation number under each temperature according to the renormalized spin-wave theory with Hatree-Fock approximations. At relatively high temperature region, there may be more than one solution, which is especially obvious in the temperature region around 34~45 K. This feature indicates the possibility of a sudden increasing of spin-wave occupations and an abrupt deduction of magnetic order, which is similar to the behavior of 1st order transition and founded in another study.[3]

Fig. S1(e) shows the evolution of spin-wave gap in the CrI_3 up to Hatree-Fock approximation. The occupations $\langle n \rangle$ increase with temperature according to eq. S9, strengthening the interactions and reduce the energies of spin-wave excitons according to eq. S8. To see the effects of interactions on spin wave spectra, we divide eq. S8 into three parts vis. the relevant high order part H_a, the relevant main part H_b and the irrelevant part H_c:

$$H_1 = H_a + H_b + H_c$$

$$H_a = \langle n \rangle \sum_{k\gamma} (J(k;\gamma\gamma) + B(k;\gamma\gamma) - J(0;\gamma\gamma) + 2A) n_{k\gamma} \qquad (S10)$$

$$H_b = \langle n \rangle \left(\sum_{k\gamma} \left\{ 2A + \sum_{\alpha} (J(0;\alpha\gamma) + B(0;\alpha\gamma)) \right\} n_{k\gamma} - \sum_{k\alpha\gamma} J(k;\alpha\gamma) b_{k\alpha}^{\dagger} b_{k\gamma} \right) \qquad (S11)$$

$$H_c = \sum_{k\gamma} A n_{k\gamma} \qquad (S12)$$

The irrelevant part H_c is constant and cannot contribute to the evolution of spin wave gap. Both the relevant parts H_a and H_b are proportional to the occupations $\langle n \rangle$. Since occupations $\langle n \rangle$ grow up with temperature, H_a and H_b also grow up with temperature, and directly decide the evolution of spin wave spectra and gap.

Form eq. S11, it is clear that H_b can be reformulated as $H_b = -\langle n \rangle H_0 / S$ (H_0 is the free part of spin wave Hamiltonian defined in eq. S6) thus is on the magnitude of H_0 and always lowers the spin wave energies. And eq. S10 shows that H_a is on the magnitude of anisotropies and its effects on spin wave energies depends on the balances of anisotropies between single-ion (A terms) and exchange intra the magnetic sublattices (B terms).

For the case of CrI_3, both exchange and single-ion anisotropies are out-of-plane preferred, and H_a is also to reduce the spin wave energies. Therefore, the spin wave gap presented in Fig. S1(e) is decreasing with temperature until the phase transition is reached.

3.2 T_C determination on QMC

Fig. S1(c) shows the evolution of 4th order Binder cumulant (U4) difference between 16x16 and 32x32 CrI_3 systems. U4 is a representative quantity for correlation length. At low temperature, U4 of two systems all approach unit since the correlations are very small, but they are different leading to finite difference. In high temperature region the correlation lengths are small too, and the spins are randomized with standard Gaussian distribution corresponding to U4=1/3, and the difference is also finite. Only on the phase transition, correlation lengths become infinite in both systems, and U4 also become the same, and the difference vanishes. Therefore, we can locate the Tc as the cross point of red and blue lines in Fig.S1(c) of CrI_3 at 49K.

3.3 $CrBr_3$ and $CrCl_3$

$CrBr_3$ and $CrCl_3$ have similar electronic and magnetic structures with CrI_3. The octahedra crystal field lifts the degeneracies in d-shell and lead to e_g and t_{2g} orbitals, as shown in Fig. S2(b) and Fig. S3(b). However, the ion radius of Br^- is smaller than I^- and Cl^- is smallest. Therefore, the overlapping between d-shell and p-shell is smaller in $CrBr_3$, and further smaller in $CrCl_3$, which are also revealed by the PDOS. Therefore, the quantity of excited states which cause the open p-shell is less in $CrBr_3$ and $CrCl_3$, and the reversed spin densities on Br and Cl are also less, as shown in Fig. S2(a) and Fig. S3(a). Hence, the super-exchanges in these two systems are weaker than CrI_3, in agreement with the DFT mapping results presented in Table 1 in main text.

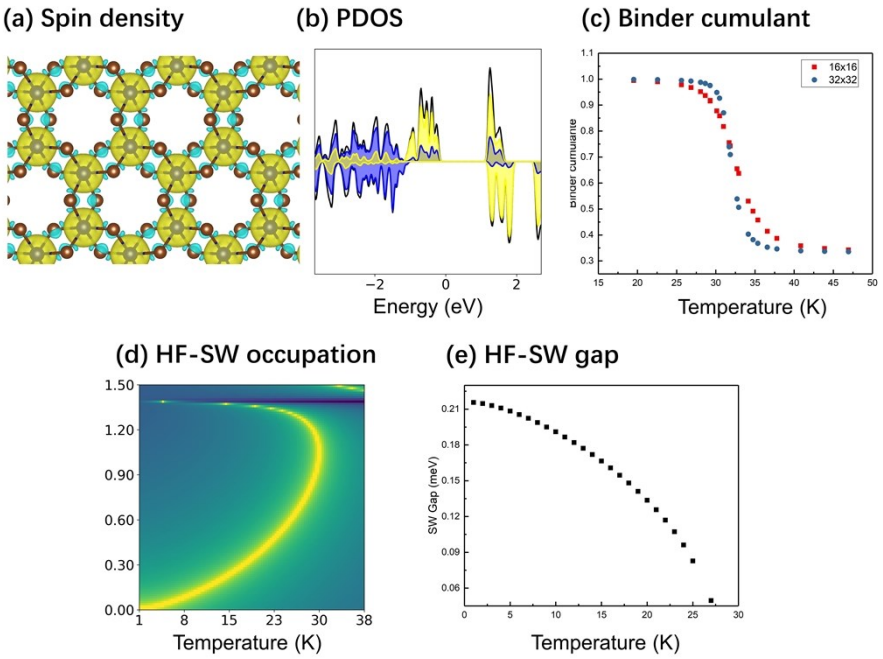

Fig. S2 (a) The spin density of $CrBr_3$, yellow and blue surfaces correspond to up- and down-spin density, respectively. (b) Projected density of states of $CrBr_3$. Blue and yellow shaded regions correspond to the DOS projected to p_{xy} and t_{2g} atomic orbitals. (c) Binder Cumulates vs. temperature obtained by QMC on 16x16 (red) and 32x32 (blue) sized $CrBr_3$ supercells. (d) Hartree-Fock renormalized spin-wave occupations and (e) spin-wave gap under each temperature for $CrBr_3$. The lightest area corresponds to the parameter space that can self-consistently solve the eq. S4-S9.

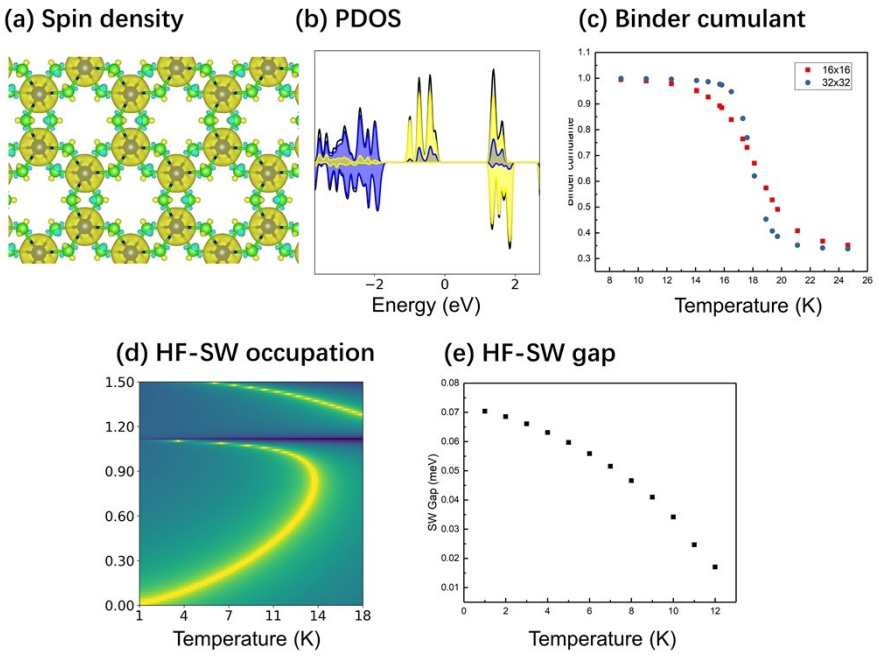

Fig. S3 (a) The spin density of $CrCl_3$, yellow and blue surfaces correspond to up- and down-spin density, respectively. (b) Projected density of states of $CrCl_3$. Blue and yellow shaded regions correspond to the DOS projected to p_{xy} and t_{2g} atomic orbitals. (c) Binder Cumulates vs. temperature obtained by QMC on 16x16 (red) and

32x32 (blue) sized $CrCl_3$ supercells. (d) Hartree-Fock renormalized spin-wave occupations and (e) spin-wave gap under each temperature for $CrCl_3$. The lightest area corresponds to the parameter space that can self-consistently solve the eq. S4-S9.

Fig. S2(d-e) and Fig. S3(d-e) show the self-consistent HF-SW occupation numbers and energy gaps under finite temperatures for $CrBr_3$ and $CrCl_3$, respectively. The evolutions presented in these two systems are similar as the CrI3 discussed before. Fig. S2(c) and Fig. S3(c) show the evolution of Binder cumulant differences along with temperature. We also located the Tc from the cross of U4, that show the Tc in $CrBr_3$ and $CrCl_3$ are 28K and 17K, respectively.

3.4 $CuCl_3$

Fig. S4(a) and (b) show the spin densities and PDOS in $CuCl_3$, respectively. In accordance with Hund's rule, we found five eighth of d-electrons of Cu^{3+} occupies every d-orbitals with spin-up states and the rest three spin-down electrons occupies t_{2g} orbitals thus revealing spin-1 on Cu^{3+} in agreement with our calculated results in Table 1 in main text. After full optimization, Cu-Cl-Cu bond angles turn out to be ~96°, revealing that the d orbitals of Cu^{3+} can overlap with px and py orbital of Cl^-. Therefore, the ferromagnetic preferred exchange coupling between Cu^{3+} can be well understood by the super-exchange mechanism, too, and the details are similar as the case of CrX_3 family. The only difference is that, since Cu^{3+} has over half-filed d-shell, the hopping p_x or p_y electrons from Cl^- should have the opposite spin-orientation to them, leading the excited state: $Cu[t_{2g\uparrow}^3 e_{g\uparrow}^2 t_{2g\downarrow}^3][p_x\text{-}e_{g\downarrow}]$ $I[p_{x\uparrow}p_{y\uparrow}]$ $[p_y\text{-}e_{g\downarrow}]$ $Cu[t_{2g\uparrow}^3 e_{g\uparrow}^2 t_{2g\downarrow}^3]$. Therefore, the final ground states will be incorporated by a part of spin-polarized Cl^- and the local states on both Cu^{3+} and Cl^- are in the same spin tunnel, as revealed by the spin-density in Fig. S4(a).

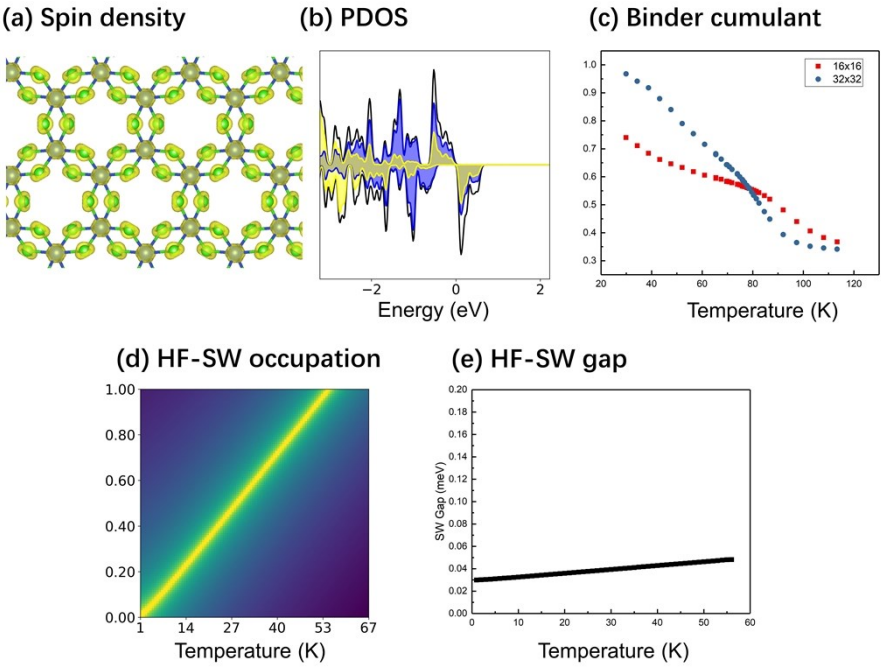

Fig. S4 (a) The spin density of CuCl3, yellow and blue surfaces correspond to up- and down-spin density, respectively. (b) Projected density of states of CuCl3. Blue and yellow shaded regions correspond to the DOS projected to pxy and t2g atomic orbitals. (c) Binder Cumulates vs. temperature obtained by QMC on 16x16 (red) and 32x32 (blue) sized CuCl3 supercells. (d) Hartree-Fock renormalized spin-wave occupations and (e) spin-wave gap under each temperature for $CuCl_3$. The lightest area corresponds to the parameter space that can self-consistently solve the eq. S4-S9.

Fig. S4(d) shows the evolution of HF-SW occupation numbers with temperatures in $CuCl_3$, and Fig. S4(e) shows the evolution of spin wave gaps. While temperature is boosted, the spin wave gap in CuCl3 is enlarged slightly. This can be understood by the behaviours of interactions encoded in eq. S8-S12. As shown in Table 1 in main text, the 2NN exchange anisotropies and single-ion anisotropies in $CuCl_3$ are in-plane preferred, the H_a part of interactions (eq. S10) thus contributes to the enhancements of spin-wave energies near the Γ-point and enlarge the spin wave gap. On the other hand, the spin wave energy gap in CuCl3 itself is very tiny, the H_b part of interactions (eq. S11) becomes inessential around Γ-point. Therefore, the whole effects of interactions lead to the increasement of spin wave energy gap as presented in Fig. S4(e).

As the result, an approximately linear relation between occupation number and temperature was found, since the growth of occupation number <n> with temperature increasing is partly impeded by the increasing of spin wave energy gap. This linear relation was also found in the MT

curve of CMC and QMC. Fig. S4(d) shows the evolution of 4th order Binder cumulant along with temperature, indicating Tc in $CuCl_3$ is 74K.

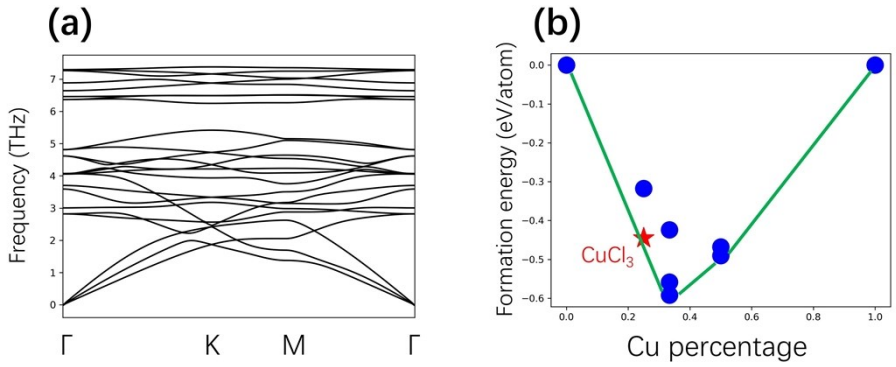

Fig. S5 (a) Phonon spectra of $CuCl_3$. (b) Formation energies of Cu-Cl binaries, each dot denotes the formation energy of one specific 2D structure that consists of Cu and Cl and the red star denotes the formation energy of CuCl3 presented in this work.

For the sake of further insuring the dynamic and thermal stabilities of the new predicted $CuCl_3$, we investigated the phonon vibrations and the formation energy hull of Cu-Cl binaries. The phonon spectra presented in Fig. S5a shows that all the phonon frequencies are above zero, indicating that the distortions in $CuCl_3$ structure are energetically costing, and the structure is dynamically stable.

Fig. S5b shows the formation energy of Cu-Cl binaries Cu_xCl_{1-x}. Formation energy is defined as $E_{form}=E(Cu_xCl_{1-x})-xE(Cu)-(1-x)E(Cl)$. $E(Cu_xCl_{1-x})$ the DFT-energy of structure Cu_xCl_{1-x}, E(Cu) the energy of FCC-Cu per atom and E(Cl) half the energy of Cl_2 molecular. The initial 2D structures of each Cu_xCl_{1-x} were obtained from C2DB[4], and were full relaxed with the same criteria as described in main text. The formation energy of our candidate $CuCl_3$ is represented by the red star that is close to the edge of formation energy hull (the green lines). Therefore, once the elements ratio is well controlled, the desired phase of $CuCl_3$ should be achieved in synthetical experiments.

3.5 $FeCl_2$

Fig. S6(a) and (b) show the spin densities and PDOS in $FeCl_2$, respectively. $FeCl_2$ has a similar structure with celebrated 2H-MoS_2, the Fe^{2+} layer is capsulated by two Cl^- layers which construct the triangular-prism crystal field. Therefore, the degeneracies in d-shell of $FeCl_2$ were lifted and dz orbital has the lowest energy, as shown in Fig. S6(b). There are six electrons in the d-shell of Fe^{2+},

and the exchange splitting in d-shell is very strong, signifying the applicability of Hund's rule. Five of the d-electrons are in spin-up states and the rest one spin down electron occupies dz orbital. The Fe-Cl-Fe bond angle is shown to be 84.6°. The detail super-exchange process which introduces the ferromagnetic exchange interactions between Fe^{2+} is similar to the case of $CuCl_3$, and the excited states with lowest energy has the electronic configurations: $Fe[d_{\uparrow}^5\ d_{z\downarrow}^1][p_x\text{-}\ d_{\downarrow}]\ Cl[p_{x\uparrow}p_{y\uparrow}]\ [p_y\text{-}\ d_{\downarrow}]\ Fe[d_{\uparrow}^5\ d_{z\downarrow}^1]$. Therefore, in the ground state of $FeCl_2$, Cl^- should have the same spin-orientation with Fe^{2+}, as revealed by the spin densities in Fig. S6(a).

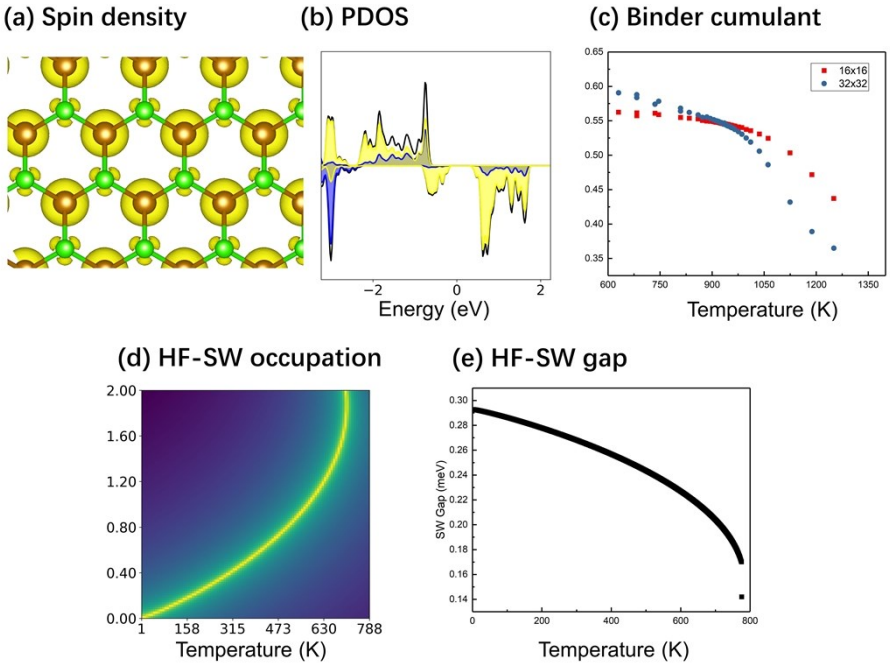

Fig. S6 (a) The spin density of $FeCl_2$, yellow and blue surfaces correspond to up- and down-spin density, respectively. (b) Projected density of states of $FeCl_2$. Blue and yellow shaded regions correspond to the DOS projected to p_{xy} and t_{2g} atomic orbitals. (c) Binder Cumulates vs. temperature obtained by QMC on 16x16 (red) and 32x32 (blue) sized $FeCl_2$ supercells. (d) Hartree-Fock renormalized spin-wave occupations and (e) spin-wave gap under each temperature for $FeCl_2$. The lightest area corresponds to the parameter space that can self-consistently solve the eq. S4-S9.

Fig. S6(d) shows the evolution of spin-wave occupation numbers with temperatures and Fig. S6(e) shows the spin wave gaps in $FeCl_2$. The thermal evolutions of spin waves in FeCl2 are close to the cases in CrX_3 family. Fig. S6(d) shows the evolution of Binder cumulant of QMC, indicating Tc in $FeCl_2$ is 931K.

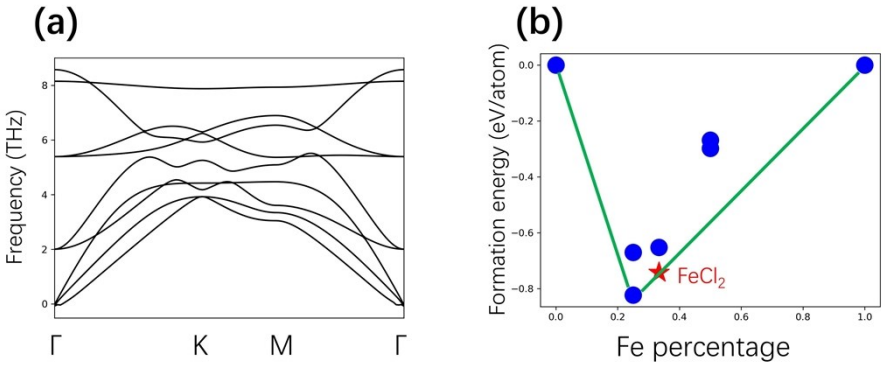

Fig. S7 (a) Phonon spectra of $FeCl_2$. (b) Formation energies of Fe-Cl binaries, each dot denotes the formation energy of one specific 2D structure that consists of Fe and Cl and the red star denotes the formation energy of FeCl2 presented in this work

Fig. S7a shows the phonon spectra of $FeCl_2$. It are clear that all the phonon vibrations in $FeCl_2$ are energetically costing, manifesting the dynamically stability of the $FeCl_2$ structure presented here.

Fig. S7b shows the formation energy of Fe-Cl binaries Fe_xCl_{1-x}, using the reference energy of FCC-Fe crystal Cl_2 molecular. The initial 2D structures of each Fe_xCl_{1-x} were also obtained from C2DB[4], and were full relaxed. The position of red star which represents the formation energy of our $FeCl_2$ structure is close to the minima of the hull and touch the border, justifying the high possibilities of realization of this predicted structure in experiments.

4. The impactions of Hubbard U applied on d-states

To identify the effects of strong correlation interactions of d-states on the magnetic properties and verify the robustness of our main results presented in main text, we employed series LDA+U calculations with U_{eff} applied on the d-states of magnetic ions and the value of U_{eff} were set to 0 eV, 1 eV and 2 eV for each candidate, which were thought to be physically reasonable.[1, 2, 5-8]

Table S1 shows the band gap of renormalized spin wave, which is the pre-requisite for 2D magnetic orders as discussed in main text. It was found that the spin wave band gaps descend along with the ascending of U_{eff} in CrX_3 family and $FeCl_2$, but behave oppositely in $CuCl_3$. All cases present opposite spin wave band gaps until U_{eff}=2eV. Therefore, the conclusions that the five

candidates present long-range ferromagnetic orders under finite temperatures were nicely preserved with the consideration of onsite U_{eff}.

Table S1. Energy gap in spin wave spectra (free from the interactions) with magnetic constants generated by LDA+U_{eff} DFT calculations.

Δ^{SW}	U_{eff}=0	U_{eff}=1	U_{eff}=2
CrI3	0.855	0.781	0.773
CrBr3	0.291	0.234	0.203
CrCl3	0.102	0.076	0.061
CuCl3	0.012	0.031	0.053
FeCl2	0.293	0.209	0.106

Table S2 shows the Tc of candidates estimated by spin wave theory. Note that Tc presented here are quantitatively different from the QMC results. As we have discussed in main text, spin wave theory only predicts phase transition coarsely. However, it is suitable to capture the qualitative trends of Tc and is sufficient for the discussions here. It shows that the Tc in the CrX_3 and $CuCl_3$ candidates are positively related to the U_{eff}. And in $FeCl_2$, the case is exactly the opposite. Nevertheless, until U_{eff}=2eV, the higher-lower order of Tc amongst all candidates never changes with the U_{eff}, and the conclusion that $CuCl_3$ and $FeCl_2$ are superior 2D FM semiconductors still holds nicely.

Table S2. Tc estimated by renormalized spin wave with magnetic constants generated by LDA+U_{eff} DFT calculations.

Tc^{SW}	U_{eff}=0	U_{eff}=1	U_{eff}=2
CrI3	44	66	81
CrBr3	27	38	44
CrCl3	12	17	20
CuCl3	56	72	83
FeCl2	776	604	377

5. Results on GGA-level

To verify our results beyond LDA functionals, we re-calculated the electronic and magnetic structures based on the functionals of general gradient approximations with Perdew-Burke−Ernzerh form[9, 10], and the key properties are listed in Table S3. Our GGA results for CrX_3 family are in line

with former studies[11-13]. And the promising high-Tc ferromagnetism in two new predicted $CuCl_3$ and $FeCl_2$ preserved on GGA-level. The distinctions between LDA and GGA are numerical, and it is apparently that the predicted Tc on GGA-level are more overestimated than LDA for the three CrX_3 systems which are experimentally known to have Tc = 45K, 28K, 17K.

Table S3. Magnetic parameters for the candidates from noncolinear DFT calculations on GGA-level. S is the maximally possible net eigenvalues of Sz. J1~ J3 are the isotropic part of 1~3 NN exchange interactions. B are the anisotropic parts of exchange interactions. Az are the single-ion magnetic anisotropies. All energy units are meV. Tc^{SW} (in kelvin) is the Curie temperature predicted by Hatree-Fock spin wave theory.

	S	J1 (B1)	J2 (B2)	J3 (B3)	Az	Tc^{SW}
CrI3	1.5	-2.87(-0.13)	-0.63(0.02)	0.17(0.00)	-0.21	84
CrBr3	1.5	-2.61(-0.03)	-0.38(0.00)	0.15(0.00)	-0.05	50
CrCl3	1.5	-1.89(-0.01)	-0.22(0.00)	0.14(0.00)	-0.01	20
CuCl3	1.0	-13.97(-0.02)	-1.40(0.00)	0.24(0.00)	0.00	83
FeCl2	2.0	-17.03(-0.02)	-0.21(-0.01)	0.04(0.03)	-0.06	976

For the experimentally known CrX3 family, the magnetic properties on hybrid functionals levels have been reported in former study[11], where the strengths of magnetic couplings and anisotropies are either stronger or comparable to the GGA-level. Therefore, we can expect that the Tc estimated on hybrid functionals levels will also significantly higher than experimental observations, at least for the CrX3 family.

Reference

1. M. Aras, Ç. Kılıç and S. Ciraci, *Physical Review B*, 2020, **101**, 054429.
2. L. Liu, S. Chen, Z. Lin and X. Zhang, *J Phys Chem Lett*, 2020, **11**, 7893-7900.
3. D. Torelli and T. Olsen, *2D Materials*, 2018, **6**, 015028.
4. S. Haastrup, M. Strange, M. Pandey, T. Deilmann, P. S. Schmidt, N. F. Hinsche, M. N. Gjerding, D. Torelli, P. M. Larsen, A. C. Riis-Jensen, J. Gath, K. W. Jacobsen, J. Jørgen Mortensen, T. Olsen and K. S. Thygesen, *2D Materials*, 2018, **5**, 042002.
5. C. Ataca, H. Şahin and S. Ciraci, *The Journal of Physical Chemistry C*, 2012, **116**, 8983-8999.
6. J. Heyd, G. E. Scuseria and M. Ernzerhof, *The Journal of Chemical Physics*, 2003, **118**, 8207.
7. V. I. Anisimov, J. Zaanen and O. K. Andersen, *Phys. Rev. B*, 1991, **44**, 943-954.
8. D. Torelli, K. S. Thygesen and T. Olsen, *2D Materials*, 2019, **6**, 045018.
9. J. P. Perdew and Y. Wang, *Physical Review B*, 1992, **45**, 13244.

10. J. P. Perdew, K. Burke and M. Ernzerhof, *Physical Review Letters*, 1996, **77**.

11. W.-B. Zhang, Q. Qu, P. Zhu and C.-H. Lam, *Journal of Materials Chemistry C*, 2015, **3**, 12457-12468.

12. J. L. Lado and J. Fernández-Rossier, *2D Materials*, 2017, **4**, 035002.

13. J. Liu, Q. Sun, Y. Kawazoe and P. Jena, *Physical chemistry chemical physics : PCCP*, 2016, **18**, 8777-8784.